Materials Science & Engineering A 791 (2020) 139700

Contents lists available at ScienceDirect

Materials Science & Engineering A

journal homepage: http://www.elsevier.com/locate/msea

Prediction of elastic-plastic deformation of nanoporous metals by FEM beam modeling: A bottom-up approach from ligaments to real microstructures

A. Odermatt [a,b], C. Richert [b], N. Huber [a,b,*]

[a] Institute of Materials Research, Materials Mechanics, Helmholtz-Zentrum Geesthacht, Germany
[b] Institute of Materials Physics and Technology, Hamburg University of Technology, Germany

ARTICLE INFO

Keywords:
Nanoporous metal
FEM beam Model
Nodal correction
Elastic-plastic deformation
FIB-SEM tomography

ABSTRACT

For the prediction of elastic-plastic deformation behavior of nanoporous materials, a computationally efficient method is needed that integrates the complex 3D network structure and the large variation of ligament shapes in a representative volume element. Finite element simulations based on beam elements are most efficient, but for a quantitative prediction, a correction is required that accounts for the effects of the mass around the junctions. To this end, a nodal correction is presented that covers a wide range of parabolic-spherical ligament shapes. Smooth functions are provided that define the extension of the nodal corrected elements along the ligament axis, their radius and their yield stress as functions of the individual ligament shape. It is shown that the increase in radius of the nodal beam elements can be replaced by scaled material parameters. Simulations of randomized FEM beam networks revealed that, in relation to the randomization of the ligament axis, the distribution of the ligament shape has a stronger impact on the macroscopic stress–strain response and should thus receive particular attention during the characterization of nanoporous microstructures. This also emphasizes the importance of the thickness analysis via image processing. Combining a nodal corrected FEM beam model with geometry data derived from image multiplication of the skeleton and Euclidean distance transform of a nanoporous gold FIB-SEM tomography dataset significantly improves the prediction of the stress–strain curve. The remaining deviation is expected to stem from the known underestimation of the real ligament diameter by the Euclidean distance transform as well as local variations in the circularity of the ligaments.

1. Introduction

Nanoporous gold (NPG) is an ideal model material for fundamental research on nanoporous metals. Macroscopic objects are produced by dealloying, exhibiting a bicontinuous network of nanoscale pores and solid ligaments connected in junctions. An overview of the fascinating morphologies and mechanical properties of this material is provided in review articles [1–3]. The average diameter of the ligaments and their connectivity density can be controlled by altering the dealloying conditions, thereby allowing to examine the impact of the ligament size, load-bearing rings, and effective solid fraction on the macroscopic mechanical properties [4–7].

Owing to the complex 3D network structure of this material, an in-depth finite element modeling of NPG is challenging. A review of the relevant literature can be found in Ref. [8]. The authors categorized the existing literature into models based on simplified unit cells with defined coordination number and ligament geometry, artificial structures generated with the help of physical or semi-physical models for a given solid fraction, and models that are derived from 3D tomography data obtained from nanoporous gold samples. A number of works deal with the simulation of the elastic-plastic deformation behavior of a real 3D microstructure of NPG, where the discussion is usually limited to results obtained for a single representative volume element (RVE) [6, 8–12].

Long before nanoporous metals drew the attention of the modeling community, extensive work has been carried out in modeling and numerical simulation of foams. Although the materials differ in various details, they have much in common. Both are open pore materials where nodes are connected with struts that vary in their thickness along their axis. The deformation mode is dominated by bending and, therefore,

* Corresponding author. Institute of Materials Research, Materials Mechanics, Helmholtz-Zentrum Geesthacht, Germany.
E-mail address: norbert.huber@hzg.de (N. Huber).

https://doi.org/10.1016/j.msea.2020.139700
Received 4 March 2020; Received in revised form 21 May 2020; Accepted 2 June 2020
Available online 13 June 2020

both communities use the Gibson-Ashby scaling laws [13,14] as common basis. The achievements in modeling of foams are a valuable basis and a perfect starting point for modeling of nanoporous metals. Early works modeled foams as 2D honeycombs incorporating the cell wall shape as an additional parameter, which allowed for analyzing the mechanical response of concave and convex shapes [15,16]. Gong et al. used a Kelvin cell model to describe the 3D network of a polyester urethane open cell foam [17,18]. According to the measured cross-sections along the length, the ligaments were considered as Euler-Bernoulli beams of various cross-sections (squares, circles, equilateral triangles, plateau borders). Due to the slenderness of the beams, the excess material of overlapping beams connecting in the nodes is normally neglected. Gong et al. removed the excess material by cutting the ends of the beams with appropriately chosen smooth curved surfaces and could show that such a correction has a considerable effect in the elastic scaling law that is predicted for non-uniform cross-sections [17]. For solid fractions of maximum 6%, the 3D FE model behaved slightly stiffer than the FEM beam model with B32 elements, which was attributed to the fact that the node geometry was somewhat different in the two models. With the idealized Kelvin cell foam, Gong et al. could assign typical geometric characteristics of the tested foams and were able to quantitatively reproduce the macroscopic compressive response [18]. In further work, this concept has been extended to larger random foam models [19]. Geometries generated with a soap model showed good agreement with the measured normalized mid-span cross-sectional area versus normalized ligament length of aluminum foams and polyester urethane foams, obtained from micro-CT generated 3D images. Simulation results for a random Kelvin cell model and the random soap model produced only a slight overprediction of 5–10% in stiffness and were able to reproduce the measured anisotropy. Jang et al. concluded that if cell anisotropy, non-uniform area distribution along the ligaments and correction for the material in the nodes are not properly represented, but the ligaments are modeled as Euler-Bernoulli beams with uniform cross sections, the moduli can be off by nearly an order of magnitude [19]. An extension toward predicting the compressive strength including elastic-plastic deformation behavior is presented in Ref. [20]. In this work, Jang et al. could show that, despite some differences in the post-limit load response and the associated localization patterns produced by the three types of models, they yield comparable elastic properties and compressive strengths. This indicates that inelastic ligament bending plays a major role in the compressive response of foams with solid fractions below 10%. While an accurate representation of the ligament bending rigidity and the base material response turned out to be essential, the effects caused by the randomness of the actual microstructure were found to be less important.

So far, the methodology for computing elastic-plastic stress–strain curves for a larger number of nanoporous metal samples with varying microstructure is essentially restricted to approaches making use of FEM beam models [21–23]. These are highly efficient, but due to the higher solid fraction around 30% their prediction accuracy is limited due to the effect of the nodal masses. In contrast to low-density foams, an additional effect is caused by the reduction of the ligaments lever length due to the larger extension of the nodal mass. This progressively increases the macroscopic strength of 3D FE model with increasing solid fraction [21]. FEM beam models do not capture this effect, because the 1D line elements of neighboring ligaments are connected at 0D junction points. The loss in stiffness in a FEM beam model is so strong that even the volumetrical overlap of the beams in the nodal region is not sufficient for its compensation. This is due to the bending moment, which applies to all beam elements over the full distance between the two junctions at both ends of a ligament. In a solid model consisting of 3D volume elements (e.g. tet or hex elements), the nodal mass around the junctions reduces the effective lever length during bending, particularly during plastic deformation, where the deformation localizes in the transition into the nodal mass [21,22]. This difference can be seen in Fig. 1, where the von Mises stress distribution for a cutout section of an NPG tomography reconstruction is shown for both modeling approaches [6,12,24]. The comparison shows that the regions that undergo plastic deformation (grey color) localize in the thin cross sections in the 3D FEM solid model (left image), whereas they are much more extended towards the junctions in the FEM beam model (right image).

A correction for considering the reduced lever length via subtracting the radius of the nodal mass at both ends from the ligament length is suggested in Ref. [21,22]. This approach is limited to correcting the macroscopic strength and is only suitable for RVEs containing identical ligaments of a simple ball-and-stick geometry. A nodal correction approach for local compensation of the softening inherent in the FEM beam model is presented in Ref. [25]. For the FEM solid model, the inherent ball-and-stick geometry is modeled as cylindrical ligaments connected in spherical nodes, representing the volume of the junctions. The authors introduce the so-called “nodal beam elements” in the FEM beam model, allowing for a quantitative predicting of both elastic and plastic deformation behavior in correspondence to the FEM solid model. For the calibration of the element properties in the nodal region as a function of the ligament aspect ratio, three parameters are required: the extension of the nodal elements along the ligament axis, l_n, their radius, r_n, and their specific Young’s Modulus, E_n. For details, we refer to Fig. 2 of [25]. Without nodal correction, all beam models considered in Ref. [25] showed a reduced stiffness and strength compared to their solid model counterparts. Following the implementation of the nodal correction, the elastic-plastic stress–strain curves are predicted up to 10% strain at an accuracy of 10% in the flow stress within a range of ligament aspect ratios $0.19 \leq r/l \leq 0.31$. This corresponds to a range of solid fractions ϕ from 0.126 to 0.31 covering the typical range of experimental values.

Apparently, independent of Jiao and Huber [25], Soyarslan et al. proposed to solve the elastic problem by increasing the Young’s modulus of the elements in the nodal region by the so-called *stiffness intensity factor* of $\omega = 40$ [26]. First of all, the striking similarity of the chosen term with the famous stress intensity factor K is inappropriate. In contrast to the well-known stress intensity factor that has an important physical meaning and founded the fracture mechanics, the *stiffness intensity factor* is not more than a fit parameter that serves to match the prediction of the FEM beam model [26] with existing results from a FEM voxel model [27]. Remarkably, the authors accept a single and surprisingly high value to hold for any solid fraction and any ligament shape. For obvious reasons, a factor of 40 in Young’s modulus leads to elements that behave almost rigidly. Furthermore, this stiffening is applied to all elements within the radius of the junction zone, which can include a significant fraction of the ligament. It can therefore be expected that this approach excessively stiffens the whole RVE.

Concerning the characterization of ligament shapes, significant progress has been made in the last five years. Pia and Delogu [28] conducted a thorough investigation of the morphologic properties of NPG and reported distributions of the shape parameters of parabolic ligaments. However, SEM images provide only information about projections of the more complex 3D ligament shapes to 2D. For an in-depth structural characterization, Hu et al. [6,11] derived RVEs of NPG for different ligament sizes via 3D FIB-SEM tomography. The RVEs are analyzed in terms of connectivity density and thickness distribution using the biggest-sphere algorithm implemented in ImageJ [29]. It is shown that the thickness distribution can be fitted by a Gaussian distribution and also that the distributions of samples with different mean ligament sizes are self-similar.

In addition to the in-depth investigation of thickness distributions, connectivity density, tortuosity, and local curvatures [6,30], the tomography data are used for setting up a FEM solid model for which the stress–strain curve is predicted assuming isotropic plasticity with linear work hardening [6,11]. Inspired by this work, Richert and Huber [12] use the same FIB-SEM tomography dataset to develop a FEM beam model. A thorough investigation of the ligament geometries revealed a high variability in the ligament length and shape. The resulting

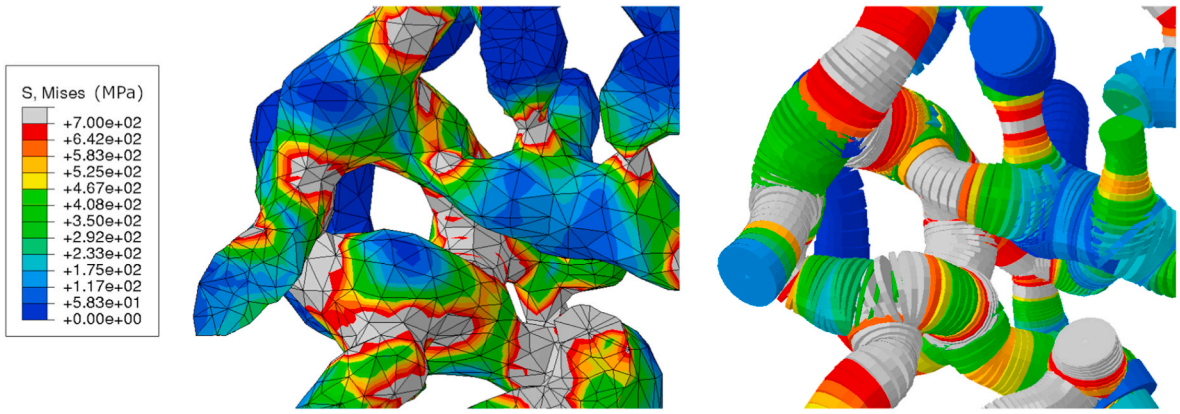

Fig. 1. Cutout of 3D FEM solid model (left) and FEM beam model (right) of NPG during macroscopic compression. The color represents the von Mises stress in MPa, whereas grey color marks regions exceeding the yield stress of 700 MPa. In comparison to the 3D FEM solid model, higher von Mises stresses are visible in the nodal regions of the FEM beam model and the plastic zones are extended towards the junctions. (For interpretation of the references to color in this figure legend, the reader is referred to the Web version of this article.)

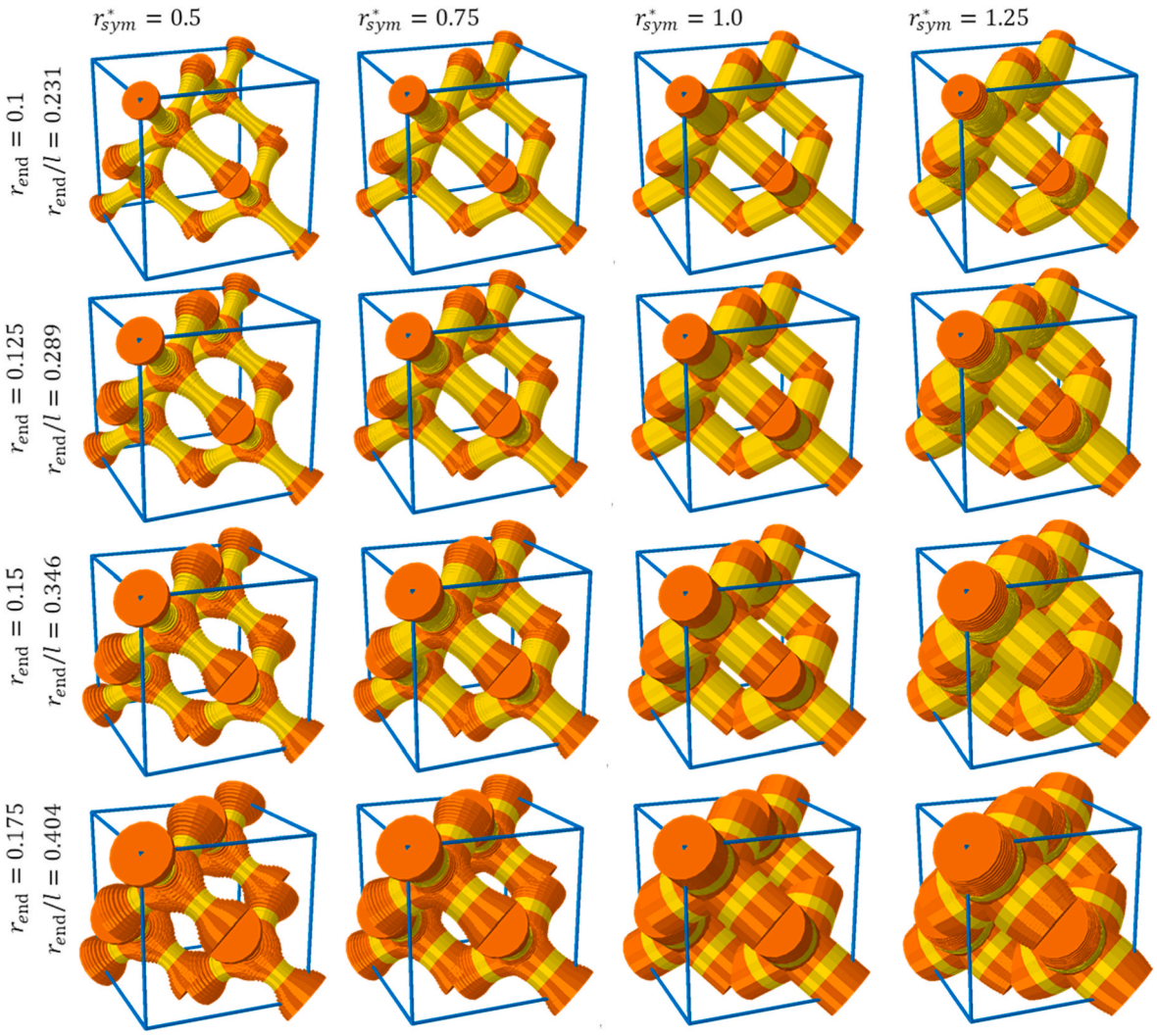

Fig. 2. FEM beam models for 16 ligament geometries according to Ref. [24]. The blue box indicates the unit cell, the orange and golden colors distinguish elements located within and outside of the spherical nodes, respectively. (For interpretation of the references to color in this figure legend, the reader is referred to the Web version of this article.)

distributions revealed mainly cylindrical, concave, and asymmetric ligament shapes, as well as a smaller fraction of convex shapes.

Furthermore, Richert and Huber investigated the effect of the thickness computation on the predicted mechanical properties and found that the stiffness and strength is significantly overestimated when the widely used biggest-sphere algorithm is used [12,24]. The degree of overestimation depends on the individual geometry of the ligament. In contrast, the Euclidian distance transform (EDT) as an alternative algorithm tends to slightly underestimate the ligament diameters as well as the resulting macroscopic mechanical properties. It is concluded that the EDT could be sufficiently accurate, supposing that the ligament cross sections are sufficiently circular [24]. Further improvements require a correction of the underestimation, e.g. by an artificial neural network approach.

The main goal of this work is to develop a nodal correction for spherical-parabolic ligament shapes, because such a parametrization is so far only available for ball-and-stick models with cylindrical ligaments connected in spherical nodes [25]. The development will be done step by step using a bottom-up approach where each step is carefully validated. This includes generalization toward concave, convex, and asymmetric ligament shapes as reported in Ref. [12], which is needed for the quantitative prediction of elastic-plastic stress–strain curves of real NPG samples. Furthermore, the accuracy in the prediction of the macroscopic mechanical response of NPG samples will be determined using the biggest-sphere and EDT algorithm for thickness estimation.

2. Finite-element models

In this section, the generalization of the nodal correction proposed in Ref. [25] is extended for the more general parabolic-spherical ligament shapes suggested by Richert and Huber [12]. This enables the FEM beam modeling approach to quantitatively predict the macroscopic stress–-strain curve for real NPG microstructures. After the calibration of the parameters for the nodal elements using symmetric ligaments, the approach will be validated for asymmetric ligament shapes as well as fully randomized shape distributions.

2.1. Geometry of ligaments

Based on the findings in Ref. [12,24], we use a parabolic-spherical ligament shape that has a smooth transition from the parabolic segment in the center of the ligament into spherical nodes, to which the ligament is attached at both ends. For the inclusion of asymmetric ligament shapes, the ends are defined by two different radii $r_{end,l}$ and $r_{end,r}$ for the left and right junction, respectively. The resulting gradient along the ligament with length l is included in Eq. (1) through parameter b. The locations $x_{Q,l}$ and $x_{Q,r}$ at which the parabolic shape transitions into the spherical parts of the ligament are determined iteratively so that a smooth ligament with a tangential transition is achieved.

$$r(x) = \begin{cases} \sqrt{r_{end,l}^2 - \left(\frac{l}{2} + x\right)^2} & -\frac{l}{2} \le x < x_{Q,l} \\ ax^2 + bx + c & x_{Q,l} \le x \le x_{Q,r} \\ \sqrt{r_{end,r}^2 - \left(\frac{l}{2} - x\right)^2} & x_{Q,r} < x \le \frac{l}{2} \end{cases} \quad (1)$$

The axial coordinate x has its origin in the mid of the ligament, so that the ligament mid radius is given by $r_{mid} = c$. For $b \ge 0$ and the right end is equal or larger than the left end, i.e. $r_{end,r} \ge r_{end,l}$. According to Ref. [24], the more general dimensionless description of the ligament shape uses the following shape parameters:

$$r_{sym}^* = \frac{r_{mid}}{\frac{1}{2}(r_{end,l} + r_{end,r})}, \quad (2)$$

$$r_{asym}^* = \frac{r_{end,r} - r_{end,l}}{\frac{1}{2}(r_{end,r} + r_{end,l})}. \quad (3)$$

In Eqs. (2) and (3), r_{sym}^* is a measure for the convexity/concavity and r_{asym}^* for the asymmetry of the ligament. From the analysis of the tomography data provided by Ref. [6,11] using the biggest-sphere thickness algorithm, the ranges of these two parameters are determined as $0.5 \le r_{sym}^* \le 1.25$ and $0 \le r_{asym}^* \le 1.5$ [12]. It is essential for a modeling approach to cover this range of shapes including asymmetric ligaments. For the special case of symmetric ligaments, we have $r_{end,l} = r_{end,r} = r_{end}$, and Eqs. (2) and (3) simplify to $r_{sym}^* = r_{mid}/r_{end}$ and $r_{asym}^* = 0$.

2.2. Representative volume elements

The representative volume elements (RVE) used for the development of the nodal correction consist of a single unit cell of a perfect diamond network containing 16 ligaments of length $l = \sqrt{3}/4$ [21]. All other lengths in this work are defined in relation to the unit cell size, which is arbitrarily chosen. For the simplicity of model generation and without restriction of generality, the unit cell size is set to 1 mm for all models discussed in this work. For a dimensionless representation, it is preferable to normalize the ligament radius to the ligament length. Therefore, in Fig. 2, the ratios r_{end}/l are also given for the 16 geometries under investigation. The ligament shapes are taken from Ref. [24], varying from highly concave ($r_{mid}/r_{end} = 0.5$) on the left side to slightly convex ($r_{mid}/r_{end} = 1.25$) on the right side of Fig. 2. In combination with the ligament end radius r_{end}, ranging from 0.1 to 0.175 from top to bottom, the solid fraction ϕ of each RVE is fixed, ranging from 8.16% to 61.61% (see Table 1 in Ref. [24]). For the computation of the solid fraction and the macroscopic properties, the volumes of the ligaments in neighboring unit cells of a periodic structure, which partially protrude into the original unit cell, are also taken into account.

The generation of the FEM beam models for Abaqus with B31 Timosheko elements in space [31] is done by Python scripting. Each ligament is represented by 20 elements, whereby the element radius is computed from Eq. (1) as a function of the local axis position x on the ligament. For the FEM solid and FEM beam models, displacement and periodic boundary conditions are used, respectively. The displacement boundary conditions represent a good approximation of the deformation that results from periodic boundary conditions. Details of the description of the model generation and boundary conditions can be found in the supplementary material provided with [23,24].

The material behavior of the solid phase is assumed to be elastic-plastic with linear isotropic hardening. Finite deformation theory is used. Consistently with [24], a Young's modulus of $E = 80$ GPa, a Poisson's ratio of $\nu = 0.42$, a yield stress of $\sigma_y = 500$ MPa, and a work-hardening rate of $E_T = 1000$ MPa are chosen for the solid phase of the RVE. The nodal correction developed in this work is based on the data obtained from the FEM solid model presented in the Supplementary Table 2 of [24].

Table 1
Nodal radius ratios, S_r, and nodal length ratios, S_l, obtained from numerical simulations and visual inspection of the elastic-plastic deformation.

	$r_{end} = 0.1$		$r_{end} = 0.125$		$r_{end} = 0.15$		$r_{end} = 0.175$	
$\frac{r_{mid}}{r_{end}}$	S_l	S_r	S_l	S_r	S_l	S_r	S_l	S_r
0.50	0.15	1.5	0.18	1.5	0.18	2.0	0.18	2.0
0.75	0.18	1.5	0.20	1.8	0.20	2.5	0.22	2.5
1.00	0.18	1.8	0.21	2.5	0.25	2.5	0.28	2.8
1.25	0.18	2.5	0.24	2.8	0.27	3.0	0.35	3.0

2.3. Mass-calibrated FEM voxel models

Since it is very difficult to model and mesh randomized geometries, FEM voxel models are used for validation. Due to the large number of 8-node HEX elements, FEM voxel models are computationally much more demanding, but they can be generated easily by scanning the FEM beam models following the approach presented in Ref. [24], supplementary material, Section 3. Thus, it is possible to compute the correct solid fraction and macroscopic response of the randomized geometries that cannot easily be built and meshed by conventional means. Richert et al. showed that a voxel resolution of 200 voxels per unit cell edge length is needed for achieving an accuracy of around 10% in the macroscopic Young's modulus [24]. This leads to high computation times and makes an elastic-plastic computation of a larger RVE, such as of size $2 \times 2 \times 2$, challenging. To give an estimate, a moderate solid fraction $\phi = 0.3$ leads to a FEM voxel model that contains nearly $2{\cdot}10^7$ HEX elements.

According to Ref. [24], the decision for a voxel being located in the solid or in the pore space is made by testing if the center point of the voxel element is located within the cylindrical volume defined by the FEM beam element. For lower resolutions, the contribution of voxels partially peeking out of the smooth convex surface increases the solid fraction relative to the correct value. This leads to a progressive increase in the macroscopic Young's modulus for decreasing the voxel resolution as seen in Fig. 8 of [24]. The same effect leads to an underprediction for dominantly concave surfaces, whereas the volume should be determined correctly for a sufficient large ensemble of plane surfaces.

Therefore, the scan method described in Ref. [24], Supplementary Section 3, is modified by adding an adjustable parameter $0.0 \leq \alpha \leq 0.5$, which is used to test the distance of the voxel center relative to the surface of the beam element. A value of $\alpha = 0.0$ corresponds to the scan as used in Ref. [24], i.e. the voxel center must lie within the FEM beam element volume or on its surface for setting a voxel as solid. For the sake of simplicity, a voxel is interpreted as an atom of a half voxel radius ($\alpha = 0.5$). In this way, it is easy to test if an atom is fully included in the beam element volume. For this value, we obtain a systematic underprediction of the solid fraction. Thus, the correct mass is obtained for a value of α between 0.0 and 0.5, depending on the ligament shape distribution in the RVE and the chosen voxel resolution, denoted by N_v.

While a low voxel resolution is mainly required for accelerating the mechanical simulation, the scan can be efficiently parallelized [24]. This allows improving the resolution for the determination of the solid fraction ϕ at an increased voxel resolution of $N_{v,scan}$. After scanning the structure with $N_{v,scan}$, the cutoff parameter α is calibrated for the lower resolution N_v. To give an example, Fig. 3 shows an RVE loaded in negative z-direction with periodic boundary conditions. It consists of linear asymmetric ligaments with $r_{mid} = 0.15$, $r^*_{sym} = 1$, and $r^*_{asym} = 0.75$. In this example, the mass calibration parameter takes a value of $\alpha = 0.32$.

The improvement by the mass calibration is shown in Fig. 3b) for FEM voxel models of $N_v = 64$ and 128 voxel resolution. The mass calibration is more effective for $N_v = 128$, because a higher resolution provides a larger number of discrete solid fractions while varying α. Overall, when we use the FEM voxel model with $N_v = 256$ as reference, it is possible to reach accuracies better than 2% and 5% in the solid fraction and the macroscopic Young's modulus, respectively, even for the low resolution voxel model with $N_v = 64$.

3. Nodal correction

3.1. Calibration of nodal beam elements

The macroscopic deformation behavior of FEM beam models generated within the experimentally observed range is compared with the corresponding FEM solid model in Ref. [24]. An overview of the results for the macroscopic Young's modulus and yield stress results is given in Fig. 4. As expected, the FEM beam models are always more compliant than the FEM solid model [21]. However, in contrast to the ball-and-stick models assumed in Ref. [25], the smooth shapes used in

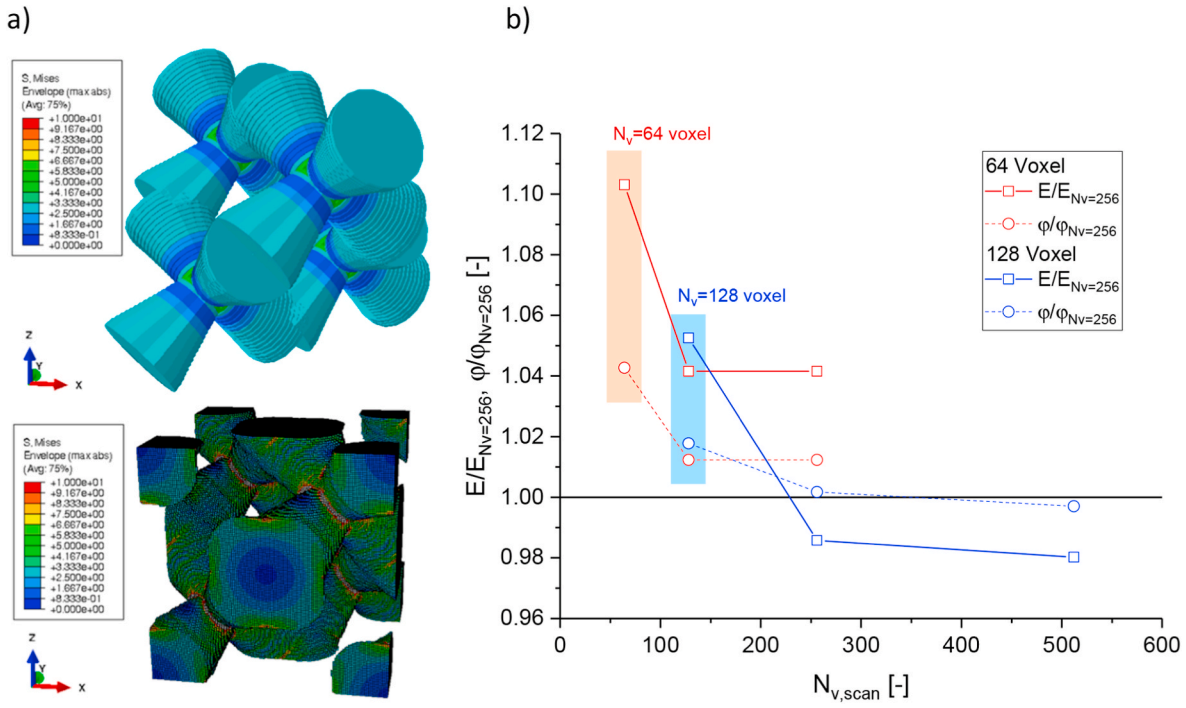

Fig. 3. Improvement of accuracy of the FEM voxel model through mass calibration: a) Stress field of a structure with asymmetric ligaments ($r_{mid} = 0.15$, $r^*_{sym} = 1$, $r^*_{asym} = 0.75$), compressed by 0.1% strain in z-direction. Shown is the FEM beam model with 20 elements per ligament and the FEM voxel model from a periodic scan of the FEM beam model with $N_v = 128$; b) Macroscopic properties computed from FEM voxel models demonstrating the improvement in the computed solid fraction ϕ and the macroscopic Young's modulus E.

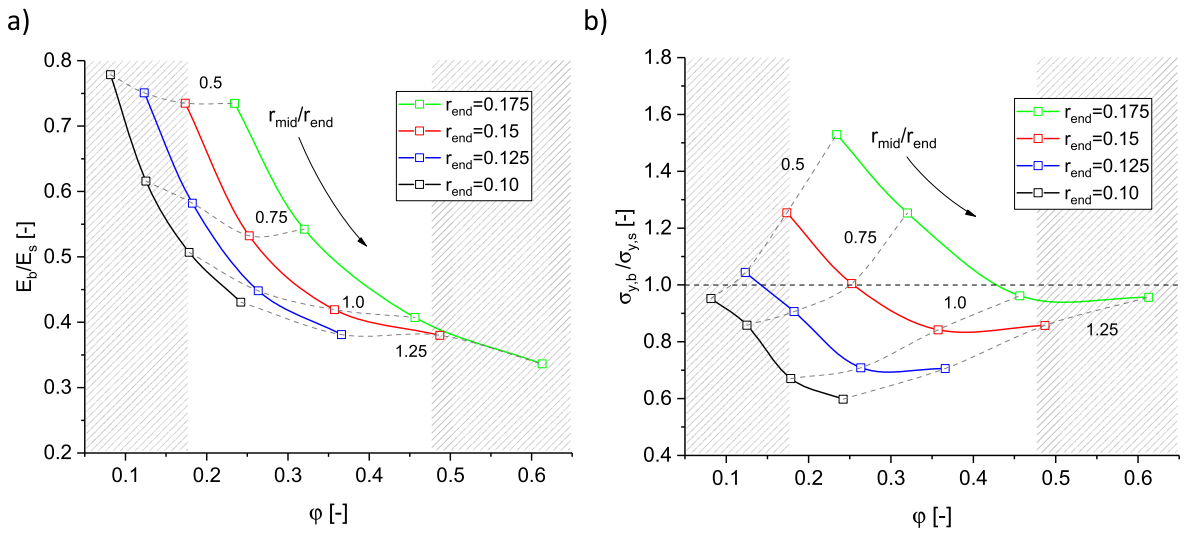

Fig. 4. Predicted macroscopic properties from FEM beam models normalized to the results from FEM solid models: a) macroscopic Young's modulus; b) macroscopic yield strength at 1% plastic strain, taken from Ref. [24].

this work can lead to a macroscopic yield stress of the FEM beam model, $\sigma_{y,b}$, below as well as above the FEM solid model, $\sigma_{y,s}$, see Fig. 4b. Throughout this work, the macroscopic yield stress is determined at 1% plastic strain.

As shown in Ref. [24], this is due to the kinematics inherent in the FEM beam elements, which cannot capture the complex deformation in the nodal region. More specifically, plastic zones in the FEM solid model develop along the tension and compression side in the thin regions of the ligaments and cross the junction volume in the middle into the neighboring ligament. In the FEM beam model, elements plasticize individually and as a whole, ensuring that cross-sectional planes remain normal to the beam axis. A partial plasticization coordinated with neighboring beam elements is desirable but not available. Therefore, the nodal correction must be able to increase the nodal stiffness, but some ligament shapes lower the yield strength. This can be solved by an independent adjustment of the elastic and plastic deformation behavior in the nodal region.

3.1.1. Elastic behavior

The principle of adjusting the beam elements is quite similar to the approach proposed by Jiao and Huber [25]. For the sampling of the radii along the ligament consisting of 21 FE nodes, the sixth FE node counted from each end was defined as the boundary of the nodal corrected region. The position of this FE node was kept variable so that the length of the nodal region can be varied. This procedure necessitates sampling of the ligament contour using Eq. (1) for the new positions of the FE nodes. This is to ensure that the nodal region of a ligament is defined by five elements. The radii of the FE nodes, which are fully contained in the nodal region, are then set to a constant value. Finally, the radius of each FEM beam element is calculated as the average of its two FE nodes radii. The nodal region then contains a transition element, which is beneficial for achieving similar deformation behavior between beam and solid models. One such ligament is shown in Fig. 5.

Fig. 6 presents the results of a systematic variation of the geometric nodal correction parameters $S_r = r_{end,n}/r_{end}$ and $S_l = l_n/l$ for ligaments with end radii $r_{end} = 0.1$ and $r_{end} = 0.125$. As can be seen, there are many possible combinations of these two parameters providing a stiffness ratio $E_b/E_s = 1.0$ (black 1.0 iso-lines). However, not every combination is meaningful. For some combinations of S_r and S_l, the localization of plastic deformation can initiate at the end of the ligament in the center of the nodal mass, which is not what is observed in the FEM solid model. When this happens, the red contour lines for $\sigma_{y,b}/\sigma_{y,s}$ show an asymptotic behavior for increasing S_r. This means that the choice of geometry parameters for the nodal corrected elements requires careful inspection of the elastic-plastic deformation of the ligament. As an additional requirement, the selected parameter combinations S_r and S_l should show a smooth trend for increasing r_{end} and r_{mid}/r_{end}.

The results of this process are listed in Table 1, and Equations (4) and (5) result from fitting these data with the SciPy curve_fit algorithm. The average stiffness ratio after the geometric nodal correction stands at 0.990 ± 0.139. The highest relative error of 15% stems from one extreme ligament geometry with the highest volume fraction, end

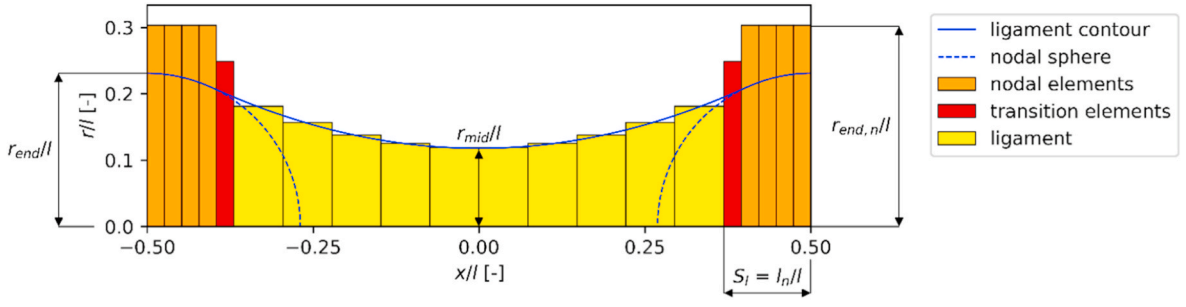

Fig. 5. Example of a geometric nodal correction $S_r = 1.25$, $S_l = 0.3$. The blue line represents the contour of the ligament and the nodal sphere. The black boxes display the beam elements after nodal correction. Five elements in the nodal region are scaled to the nodal length l_n; the first four are set to $r_{end,l}$. The 10 elements of the ligament are equally distributed and set to the ligament radius $r(x)$. The red transition element radius averages the radii of the ligament end and nodal region. (For interpretation of the references to color in this figure legend, the reader is referred to the Web version of this article.)

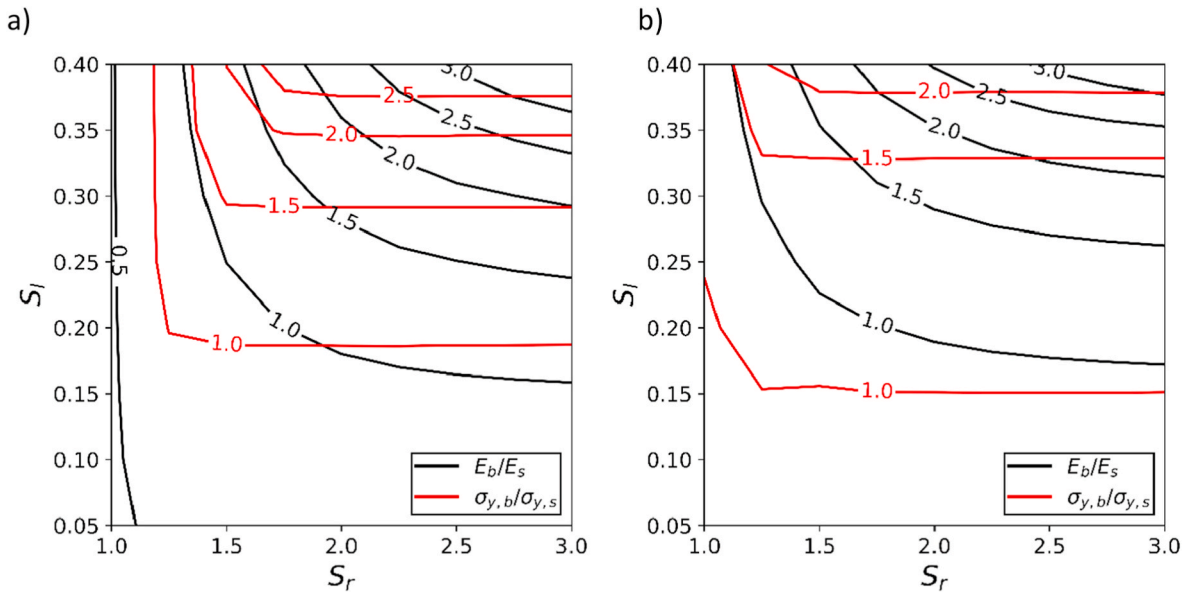

Fig. 6. Systematic variation of nodal radius and length ratios for two selected ligament geometries. Contour lines of the ratios for FEM beam to solid for the macroscopic Young's modulus (black curves) and macroscopic yield strength (red curves): a) $r_{end} = 0.1$ and $r_{mid}/r_{end} = 1.0$; b) $r_{end} = 0.125$ and $r_{mid}/r_{end} = 0.75$. (For interpretation of the references to color in this figure legend, the reader is referred to the Web version of this article.)

radius, and ligament shape factor ($r_{end} = 0.175$, $r_{mid}/r_{end} = 1.25$), while the average error of 3.4% is fairly low.

$$S_r = -18.75\left(\frac{r_{end}}{l}\right)^2 + 16.411\frac{r_{end}}{l} + 0.4\left(\frac{r_{mid}}{r_{end}}\right)^2 + 0.72\frac{r_{mid}}{r_{end}} - 1.948 \quad (4)$$

$$S_l = -0.188\left(\frac{r_{end}}{l}\right)^2 + 0.591\frac{r_{end}}{l} + 0.01\left(\frac{r_{mid}}{r_{end}}\right)^2 + 0.1\frac{r_{mid}}{r_{end}} - 0.048 \quad (5)$$

3.1.2. Plastic behavior

As Fig. 4b) shows, for some of the ligament geometries, the strength of the FEM beam model is higher than that of the corresponding solid model, whereas the macroscopic stiffness is lower. It is therefore necessary to increase the stiffness while simultaneously lowering the strength via the nodal correction. Furthermore, in Fig. 6b) no intersection of the 1.0 contour lines of the strength and stiffness ratios can be found. This can only be solved by a combination of two individual correction components: (1) A geometric nodal correction that increases the elastic stiffness and (2) a nodal corrected yield stress that independently adjusts the resistance against plastic flow. For this purpose, a common scale factor S_{σ_y} for the nodal plastic properties, defined by the nodal yield strength $\sigma_{y,n}$ and nodal work hardening rate $E_{T,n}$ is introduced.

Knowing that the deformation in NPG is controlled by bending [21], the critical stress in the beam element is given by

$$\sigma = M_b/W, \quad (6)$$

where M_b is the bending moment, and the section modulus W for circular cross sections is

$$W = \frac{\pi}{4}r^3. \quad (7)$$

Therefore, the bending strength in the nodal region scales linearly with S_r^3 and $(1 - S_l)$, because the bending moment M_b reduces linearly as the extension of the nodal region increases. Based on this, we propose a scaling of the yield strength and the work hardening rate in the nodal region according to

$$\sigma_{y,n} = S_{\sigma_y} \cdot \frac{1}{S_r^3(1 - S_l)} \cdot \sigma_{y,s}, \quad (8)$$

$$E_{T,n} = S_{\sigma_y} \cdot \frac{1}{S_r^3(1 - S_l)} \cdot E_{T,s}. \quad (9)$$

Finally, the data listed in Table 2 can be described by the fit function

$$S_{\sigma_y} = 0.582\left(\frac{r_{end}}{l}\right)^2 - 2.936\frac{r_{end}}{l} - 0.317\left(\frac{r_{mid}}{r_{end}}\right)^2 + 3.334\frac{r_{mid}}{r_{end}} + 0.043. \quad (10)$$

It allows for calculation of the nodal yield strength scale factor, for which the average strength ratio of the nodal corrected FEM beam model to FEM solid model is 1.004 ± 0.107. The highest relative error in the strength ratio is 11.1%, whereas the average error is 3.1%.

3.2. Validation and generalization

The approach for the nodal correction presented in Section 3.1 is developed for idealized RVEs, comprising 16 identical, perfectly symmetric ligaments organized in a diamond lattice. The objective here is to

Table 2
Parameters for plastic nodal correction.

	$r_{end} = 0.1$		$r_{end} = 0.125$		$r_{end} = 0.15$		$r_{end} = 0.175$	
r^*_{sym}	$\frac{\sigma_{y,n}}{\sigma_{y,s}}$	$S_{\sigma_{y,n}}$	$\frac{\sigma_{y,n}}{\sigma_{y,s}}$	$S_{\sigma_{y,n}}$	$\frac{\sigma_{y,n}}{\sigma_{y,s}}$	$S_{\sigma_{y,n}}$	$\frac{\sigma_{y,n}}{\sigma_{y,s}}$	$S_{\sigma_{y,n}}$
0.50	0.521	1.000	0.182	0.735	0.107	0.642	0.082	0.580
0.75	0.572	2.000	0.246	1.583	0.158	1.415	0.118	1.216
1.00	0.352	2.163	0.228	2.313	0.160	2.142	0.126	1.897
1.25	0.289	3.000	0.191	3.000	0.137	2.725	0.125	2.730

isolate the deformation behavior of a ligament-node connection of a well-defined shape, while the boundary conditions are defined by the ligament network as a response to an external deformation of the RVE. As all half ligaments in the RVE resemble identical deformation and stress fields along their axis, we can assume that the identified nodal correction generally holds and can be implemented in any ligament network of higher complexity by the interpolation of the nodal correction parameters to the geometry of each individual half ligament. This will be demonstrated in the following.

3.2.1. Transferability of beam geometry and material parameters

According to Eqs. (6) and (7), we can write a nodal corrected beam element as $M_b = \sigma W_{nc}$, with $W_{nc} = W S_r^3$. If we keep the bending moment M_b effectively constant, a modification of the nodal corrected section modulus W_{nc} into its original value W requires an inverse proportional modification of the stress measure. Therefore, it is possible to map the nodal correction parameters S_r as computed from Eq. (4) to nodal corrected material parameters P_{nc} according to

$$P W_{nc} = P_{nc} W, \quad P \in \{E, \sigma_y, E_T\}, \tag{11}$$

or

$$P_{nc} = P S_r^3, \quad P \in \{E, \sigma_y, E_T\}. \tag{12}$$

Therefore, the two strategies of increasing the element radius or the material properties in the nodal region are interchangeable. This is demonstrated with simulations for the 16 geometries shown in Fig. 2 (diamond symbols in Fig. 7). Compared to the substantial deviations between the uncorrected FEM beam model and the FEM solid model seen in Fig. 4, the agreement of the two nodal corrections is remarkable and within the overall scatter.

Equation (12) implies that the geometric nodal correction by Jiao and Huber [25] and the *junction zone strategy* proposed by Soyarslan et al. [26] are mutually transferable, for which the *junction zone strategy* is reduced to a special case of the nodal correction [25], limited to elasticity. In addition to the results from this work, Fig. 7a) contains also predictions based on the *junction zone strategy*. Applying $\omega = 40$ systematically overpredicts the macroscopic stiffness of the RVE for all ligament shapes by minimum +15% and up to +180%. As a result of an iterative calibration, the value $\omega = 3.7$ could bring the average error for all 16 ligament geometries down to zero, but the data still scatter from −28% to +56% below and above the target value (open orange circles in Fig. 7a). This means that the value $\omega = 40$ is more than a factor of 10 too high.

A quantitative comparison of the size of the nodal corrected region can be achieved by translating $\omega = 40$ to our nodal correction parameters developed in Section 3.1.1. Solving Eq. (12) with respect to S_r and inserting $E_{nc}/E = \omega$ for P_{nc}/P yields $S_r = \sqrt[3]{40} = 3.42$. This value is applied to all FE elements in the junction zone, displayed in orange in Fig. 2, i.e. the second geometric parameter, the nodal length, equals the ligament end radius $S_l = r_{end}/l$. Fig. 8 compares both values with the nodal correction parameters represented by Eqs. (4) and (5). The plots confirm that setting the nodal corrected elements to the geometry values as derived from the work of Soyarslan et al. leads to significantly oversized element radii as well as nodal lengths. For nearly all concave ligament shapes, which represent the majority in NPG, both the nodal length and the radius are more than a factor 2 too large, causing the systematic overprediction of the macroscopic stiffness in Fig. 7a). For the higher solid fractions, only a few deformable elements are left (marked in golden in Fig. 2). Therefore, apart from the fact that a single value is not applicable to the diverse ligament shapes present in NPG, our results disprove the high value of the *stiffness intensity factor* $\omega = 40$, as determined in Ref. [26].

3.2.2. Random ligament shapes and variation of plastic properties

Next, we investigate the validity of the nodal correction for randomized RVEs of size 2 × 2 × 2 and varying flow stresses. The radius at the ligament ends is chosen randomly within the limits of the developed nodal correction, i.e. $r_{end} = 0.135 \pm 0.035$. Node radii at the boundaries are copied so that periodic boundary conditions can be applied to the RVE. Subsequently, random setting of $r_{mid}/r_{end} = 0.8 \pm 0.3$ defines the curvature of the ligaments. Effectively, all relevant shapes including concave, convex, and asymmetric ligaments are included, as shown in Fig. 9.

An FEM voxel model of resolution $N_v = 128$ is generated from the FEM beam model by scanning and mass calibration, as described in Section 2.3. For this RVE, the plastic material parameters are systematically varied via job number j according to $\sigma_{y,s} = j \cdot 200$ MPa, $E_{T,s} = j \cdot 1000$ MPa in 5 steps, i.e. the yield strength and the work hardening rate range from 200 to 1000 MPa and 1000 to 5000 MPa, respectively. This gives an impression of how general the nodal correction is also in terms of varying ratios $\sigma_{y,s}/E_s$ and $E_{T,s}/E_s$. It can be seen that the predicted elastic behavior and the yield strength is in excellent agreement, whereas with increasing plastic strain the FEM beam model tends to overpredict the response of the FEM voxel model. Nevertheless, compared to the uncorrected FEM beam model (dashed curves), the

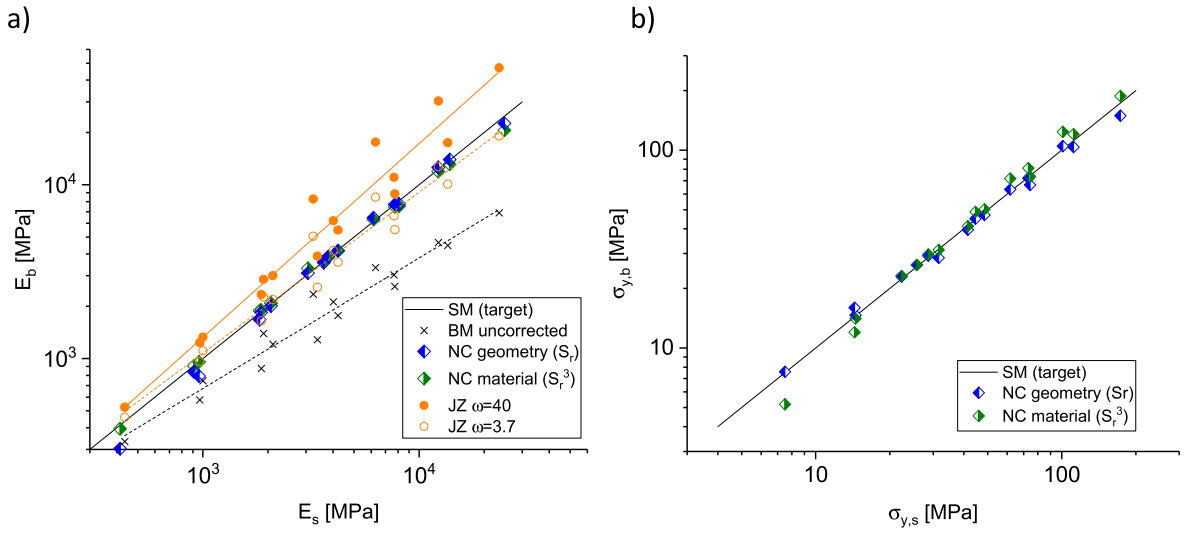

Fig. 7. Validation of the nodal corrected beam model for perfectly symmetric RVEs of size 1 × 1 × 1: a) macroscopic Young's modulus E_b; b) macroscopic yield stress $\sigma_{y,b}$. Abbreviations denote FEM solid model (SM), FEM beam model (BM), nodal correction from this work (NC), junction zone strategy (JZ) according to Ref. [26].

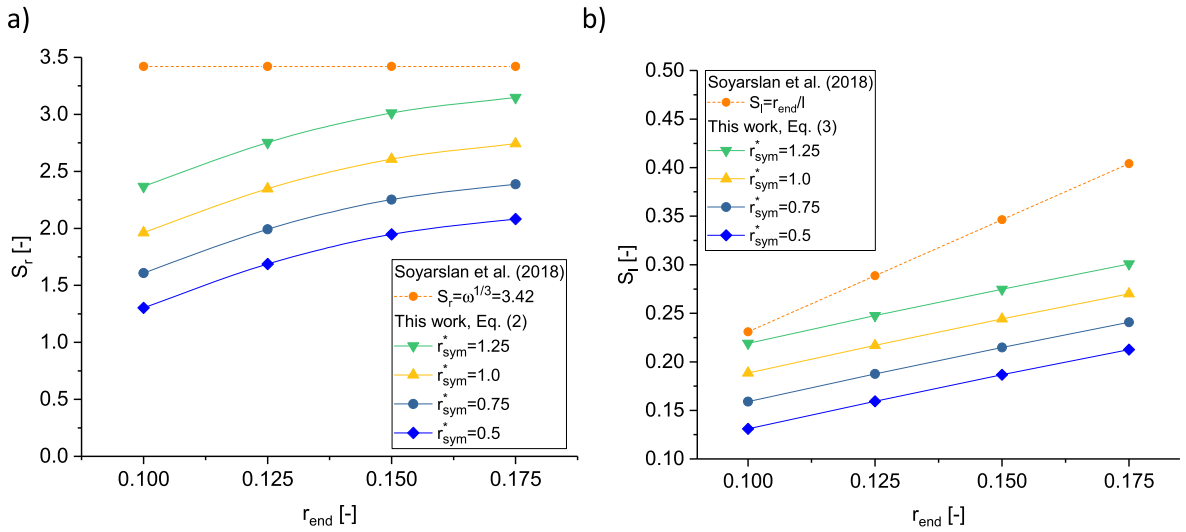

Fig. 8. Comparison of nodal correction parameters with corresponding values from the junction zone strategy [26] as a function of ligament end radius r_{end} and ligament shape r^*_{sym}. In all cases, the junction zone strategy leads to significantly larger nodal lengths and radii. a) nodal radius factor $S_r = r_{end,n} / r_{end}$; b) nodal length factor $S_l = l_n/l$.

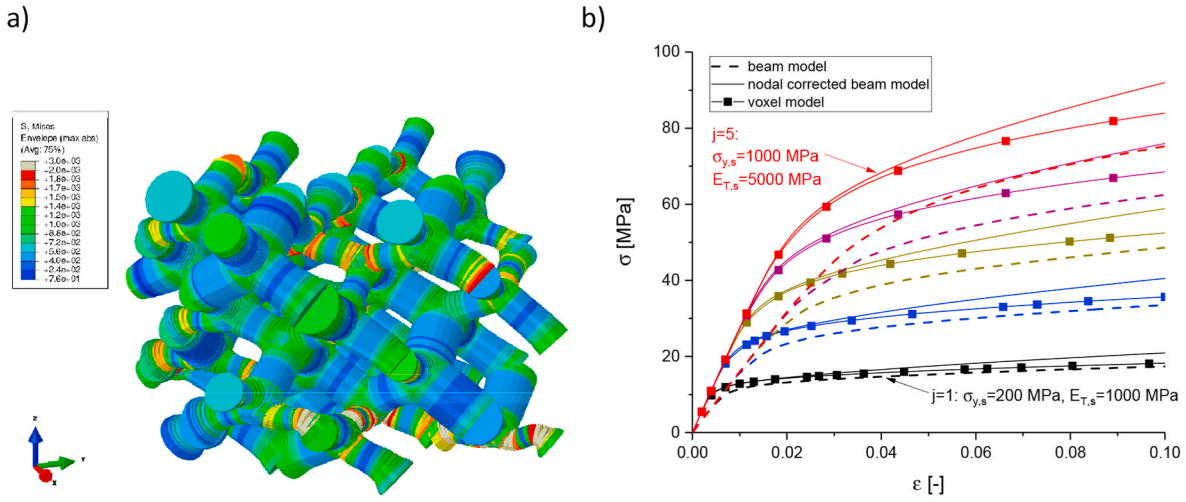

Fig. 9. Periodic RVE of size 2 × 2 × 2 with random ligament shapes: a) von Mises stress distribution for job number 2 after compression to 20% strain; b) stress–strain curves predicted with variation of yield stress $\sigma_{y,s}$ and work hardening rate $E_{T,s}$ in the range from 200 to 1000 MPa and 1000 to 5000 MPa, respectively.

overall accuracy is very good across all strength levels.

4. Approaching NPG microstructure

Moving closer toward real microstructures, the nodal correction is tested with randomized structures as proposed in Ref. [21,22]. Finally, the approach is tested for FIB/SEM tomography data provided by Hu et al. [6,11].

4.1. Randomized diamond structures

In this section, the degree of complexity in the geometry is successively increased. We start from a fully connected diamond structure where all ligaments have the same shape while the ligament axis paths show an increasing degree of randomization. The randomization approach [21,22] uses parameter A, which defines the range of random displacement applied to each junction FE node, distorting the initial ligament network. For a fully connected diamond structure, the value $A = 0.23$ reproduces the experimentally measured Poisson's ratio [22]. However, for decreasing connectivity density, the value of A can be significantly lower [23].

Against our expectations, simulations for randomized structures revealed that the established randomization approach does not soften the stress–strain curves computed for the FEM voxel models. By randomly shifting the junctions, ligaments are stretched and aligned when the common junction is pulled away. This happens already at low degrees of randomization $A \gtrsim 0.1$ and leads to the merging of ligaments, which are oriented in a V-shape. The resulting increase in structural stiffness and strength compensates for the effect of randomization.

In order to achieve more realistic geometries that are characterized by ligaments leaving junctions sufficiently normal to the nodal mass, the randomization approach has been modified. Instead of shifting each junction FE node, a randomly picked FE node in the middle region of each ligament at position $\frac{x}{l} \in [-0.25,\ 0.25]$ is shifted normal to the axis at a random angle and amplitude $A_l = cA$. The constant $c = 0.625$ is calibrated to reproduce the macroscopic Young's modulus in the range $0 \leq A \leq 0.3$ [22]. Because of the much stronger curvature of the ligaments, the new randomization yields larger values for the macroscopic Poisson's ratio ν_{lig}, which can be related to the values for displacing

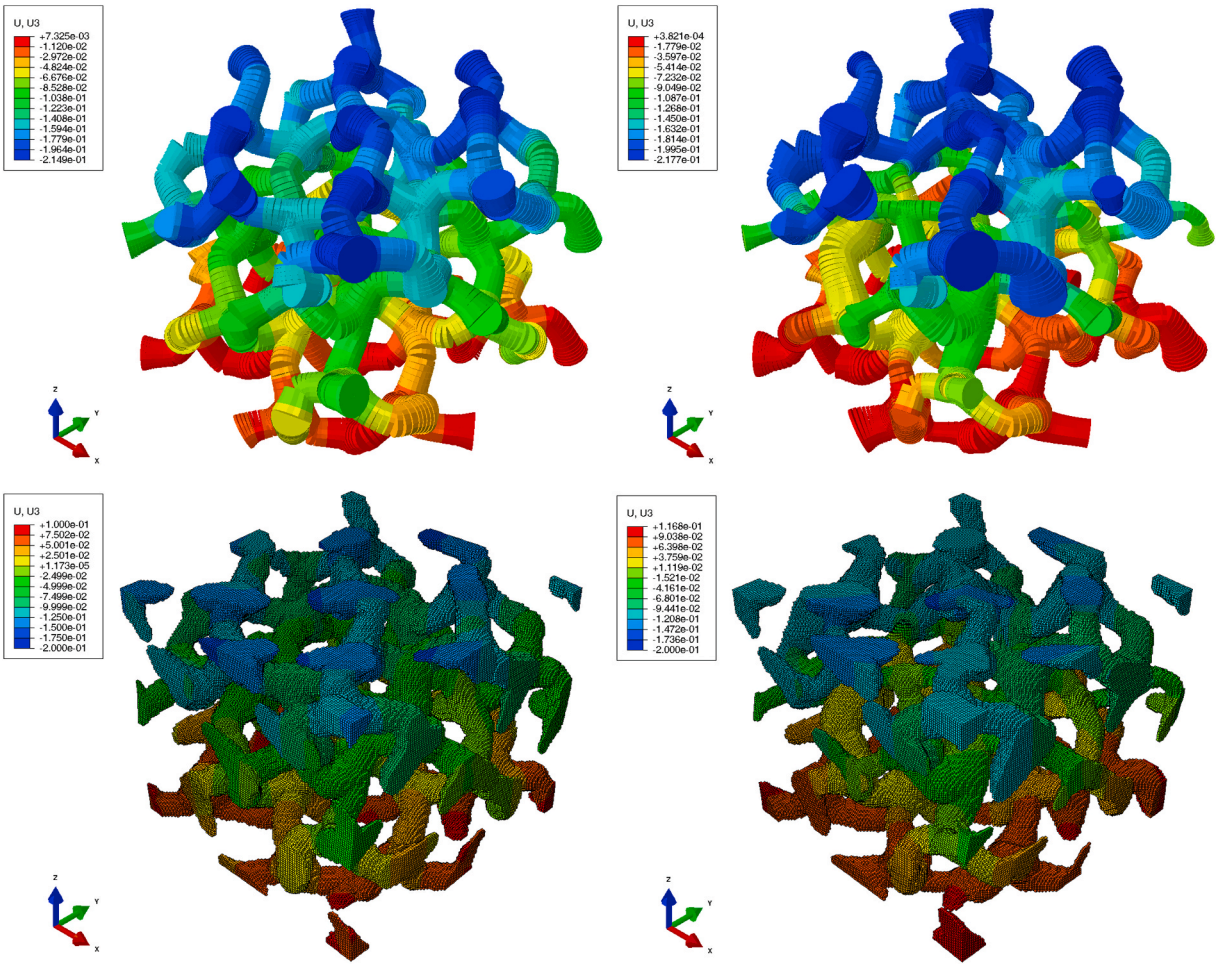

Fig. 10. FEM beam models (top) and FEM voxel models (bottom) of randomized microstructures for RVE size 2 × 2 × 2. Color displays deformation in z-direction after 10% compression: a) $A = 0.2$, $r_{end} = 0.12$, $r^*_{sym} = 0.75$; b) $A = 0.2$, $r_{end} = 0.12 \pm 0.04$, $r^*_{sym} = 0.7 \pm 0.2$. (For interpretation of the references to color in this figure legend, the reader is referred to the Web version of this article.)

junctions ν_{jct} by a quadratic dependency $\nu_{lig} = \nu_{jct} + 0.13A + 0.65A^2$.

An advantage of the modified randomization method is that it allows applying periodic displacement boundary conditions to the junction FE nodes located at the surface of the RVE while randomly distorting the structure. Fig. 10 exemplarily presents FEM beam models and FEM voxel models for the largest randomization value $A = 0.2$. While in Fig. 10a)

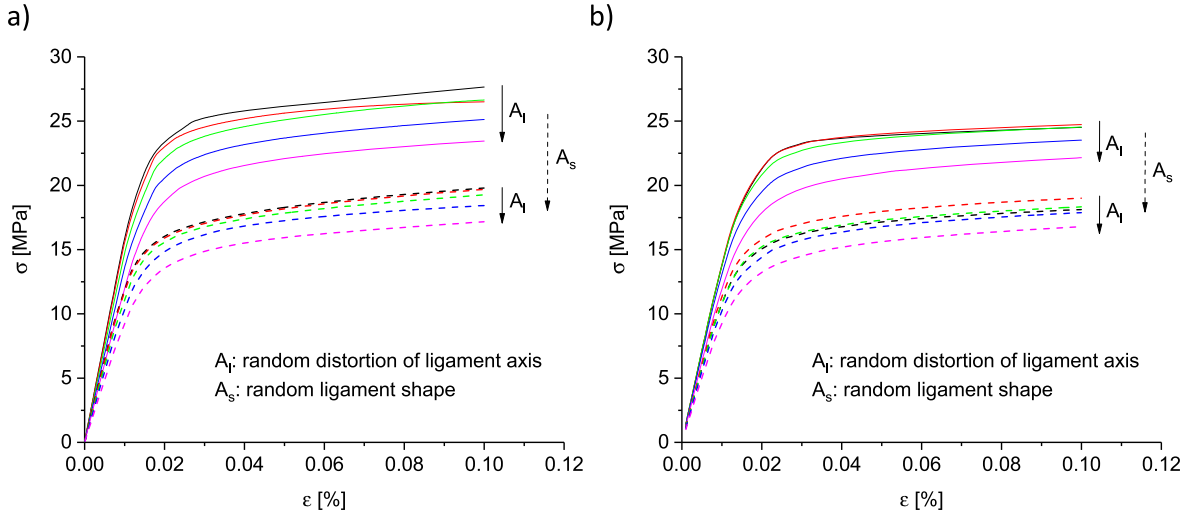

Fig. 11. Macroscopic stress–strain curves predicted for randomized microstructures. Periodic RVEs of size 2 × 2 × 2 are randomized by normal shift of a ligament mid-node by A_l, ranging from 0 to 0.125; randomization of ligament shapes is qualitatively indicated by A_s. Results are presented for a) nodal corrected FEM beam model and b) FEM voxel model.

identical ligament shapes are applied, the microstructure of Fig. 10b) contains random ligament shapes. The random set of ligament shape parameters $r_{end,l}$, $r_{end,r}$, and r_{mid} generated for each ligament at $A = 0$ can be stored and loaded for setting up all structures with $A > 0$ with the same shapes.

Fig. 11a) shows the results for nodal corrected FEM beam models with RVEs of size $2 \times 2 \times 2$, compressed to 10% strain using periodic boundary conditions. First, the ligament shape is chosen identical for all ligaments by $r_{end} = 0.12$ and $r^*_{sym} = 0.75$, shown as solid curves. As expected, the stiffness and strength decrease for an increasing degree of randomization A from 0 to 0.2 varied in increments of 0.05. With increasing randomization, the solid fraction increases from $\phi = 0.162$ to 0.220 due to the increasing arc length of the ligaments [22]. For the very same ligament axis paths, simulations with randomized ligament shapes are added as dashed curves. The ranges for the random selection of the ligament shapes are chosen within $r_{end} = 0.12 \pm 0.04$ and $r^*_{sym} = 0.7 \pm 0.2$, fulfilling the condition that the resulting solid fractions match the values of the structures with constant ligament shape within 5% accuracy. It is evident from Fig. 11a) that the randomization of the ligament shape (A_s) leads to a stronger loss of stiffness and strength than does the randomization of the ligament axis (A_l). Furthermore, for randomized ligament shapes, the effect of structure randomization via the parameter A_l is reduced. Therefore, the ligament shape distribution has higher importance and should receive particular attention during the characterization of the microstructure of NPG. This once more emphasizes the key role of the thickness algorithms in image processing [12,24].

The predictions by the nodal corrected FEM beam models are supported by the results from FEM voxel models (Fig. 11b). Comparing the plots in Fig. 11a) and b), it can be seen that the effect of randomization of the ligament axis through A_l is further reduced for the FEM voxel models. This mainly results from a higher probability that volumes of distorted ligaments merge in the vicinity of junctions, leading to stiffening and strengthening of the connections and partially compensating for the softening effect caused by the randomization.

4.2. Predictions for NPG tomography

The ultimate goal is to apply the nodal corrected FEM beam model to the microstructure of a real NPG sample, as provided by Hu et al. [6,11]. For the details on the generation of the FEM beam model from the tomography dataset, we refer to Refs. [12,24]. Of particular interest are FEM beam models that are based on the thickness algorithms established in the literature, which are the *biggest-sphere thickness* algorithm (Th) [29] and the *Euclidean distance transform* (EDT) implemented in ImageJ [32]. While the *biggest-sphere* algorithm systematically overpredicts the diameter of the ligaments in NPG, the *EDT* shows some systematic underprediction. As the FEM beam model is built on Bezier fits of the skeleton network, each ligament can be easily interpolated to 20 elements, for which the incorporation of the nodal correction can use the same coding as that used for the diamond structures in previous sections.

The predictions from the FEM beam models with and without nodal correction are presented in Fig. 12a) compared to the stress–strain curve of the FEM solid model provided by Ref. [6]. In this simulations, symmetry boundary conditions and material parameters are applied as described in Refs. [12,24], i.e. we used a Young's modulus of $E_s = 81$ GPa, Poisson's ratio $\nu_s = 0.42$, yield stress $\sigma_{y,s} = 700$ MPa, and work hardening rate $E_{T,s} = 1000$ MPa. The overprediction from the nodal corrected FEM beam model based on the *biggest-sphere thickness* algorithm (Th) is expected. The result shows how strong the overprediction of the *biggest-sphere thickness* algorithm effectively reflects in the macroscopic response of the material. On the lower side, the results for the EDT turn out to be very close to the FEM solid model. The initial deviation before nodal correction is about −40%, which is reduced to −22% by the nodal correction. The remaining gap between the nodal corrected stress–strain curve and the solid model can be explained from the trend of EDT to yield a slight underestimation of the ligament diameter. Further effects contributing to this deviation can originate from ligaments in NPG that deviate from circular cross sections. Neighboring ligaments that merge close to the junction, as found in our artificial randomized geometries in Section 4.1, might also raise the curve of the solid model relative to the beam model.

Fig. 12b) compares the deformation field for the FEM beam model (EDT), which is fully visible at the left side, overlaid with the corresponding FEM solid model fully visible at the right side. To limit the view to a small number of ligaments, the model is cut to 25% of its original size in out-of-plane y-direction. The color indicates the vertical displacement field in z-direction with the maximum compression in blue near the top face and zero/positive displacements (red/grey) at the bottom. The overlay of the beam model and the solid model allows simultaneously comparing ligament axis, thickness, and their local deformation by location and color. Although the EDT underestimates the thickness of the ligaments in several places, the overall good agreement confirms that the nodal corrected FEM beam model predicts

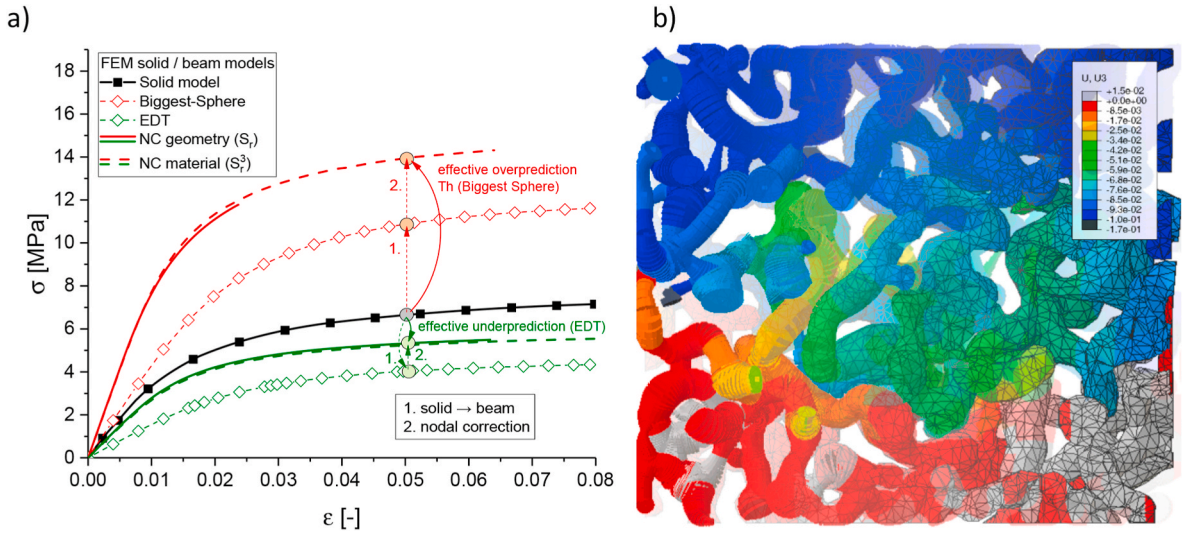

Fig. 12. Comparison of predictions by FEM beam models with FEM solid models [6]. a) Stress–strain curves; b) deformation of the microstructure after 10% compression. Colors indicate the magnitude of displacement in the direction of compression. Nodal corrected results are denoted by NC, see Section 3.2.1. (For interpretation of the references to color in this figure legend, the reader is referred to the Web version of this article.)

the local deformation field in hitherto unequal agreement with the FEM solid model, see Refs. [12,24].

5. Conclusions

Based on previous works on ball-and-stick models [25], a generalized nodal correction for FEM beam models is presented that covers a wide range of parabolic-spherical ligament shapes [24]. The challenge in the calibration of the nodal element geometry and material parameters was to provide a solution for the contradictive requirements of elastic stiffening and strength softening. This is due to the limitations of the kinematics of FEM beam elements that lock the plastic deformation in the junction volumes [24].

Second-degree polynomial fit functions are provided for the calculation of the nodal correction parameters that depend on the two parameters defining the ligament shape, namely the mid-to-end radius ratio r_{mid}/r_{end} and the end radius-to-ligament length ratio $r_{end}/\ l$. With these functions, the extension of the nodal corrected elements along the ligament axis, their radius and their plastic material parameters are determined in relation to the original ligament shape and yield stress.

It could be shown that the radius increase in the nodal region can be translated into elastic and plastic material parameters by scaling with an exponent of 3 according to the well-known relations of beam mechanics. This allows for the implementation of a local nodal correction based on mechanical properties so that the ligament geometry remains unchanged. Furthermore, the generality of the nodal correction approach was successfully demonstrated by testing large variations of the strength-to-stiffness ratio in the mechanical properties as well as the randomization of the RVE and ligament shape. Making use of the interchangeability between nodal corrected geometry and material parameters, our results disprove the *junction zone strategy* [26]. Depending on the ligament shape, their approach systematically overpredicts the macroscopic stiffness by 15% to 180%. For the 16 geometries discussed in this paper, the value $\omega = 40$ [26] is more than a factor of 10 too high.

Concerning the randomization of the RVE, the approach presented in Ref. [21] is modified to a random shift of ligament nodes normal to their axis. This avoids unwanted and unrealistic merging of ligaments close to the junctions in the FEM voxel models, which would compensate or even overcompensate for the desired softening known for randomized structures. Simulations with randomized structures and ligament shapes show that the randomization of the ligament shape leads to a stronger loss of stiffness and strength compared to the randomization of the ligament axis. Furthermore, for random ligament shapes, the effect of the randomization of the ligament axis is decreasing. The reduction is even more pronounced for FEM voxel models, where the effect of volumetric overlaps of randomized ligaments is correctly considered. It is concluded that the ligament shape distribution is of major importance and should receive particular attention during the characterization of the microstructure of NPG, emphasizing the important role of thickness estimation during image processing [12,24].

Finally, the developed nodal correction was implemented into the FEM beam model generated from FIB-SEM tomography of NPG [6,12,24]. Stress–strain curves are computed for ligament diameters as determined with the *biggest-sphere thickness* algorithm and the *Euclidean distance transform* (*EDT*) algorithm. As expected, the stress–strain curve using the *biggest-sphere thickness* data overpredicts the curve from the FEM solid model by a factor of 2. In contrast, the stress–strain curve for the *EDT* data is shifted much closer toward the solid model, reducing the deviation from −40% without nodal correction to −22% with nodal correction, a hitherto-unequalled agreement with the FEM solid model. The remaining gap between the nodal corrected stress–strain curve and the solid model is explained from the property of the EDT to slightly underestimate the ligament diameter, as the NPG ligament shapes show highly varying diameters along their axes. As pointed out in Ref. [24], the original ligaments could show some deviations from the assumed simplified circular cross sections. Furthermore, in random structures, neighboring ligaments can merge close to the junction, causing mechanical stiffening and strengthening. This cannot be captured by the FEM beam model.

Funding

This work was supported by the Deutsche Forschungsgemeinschaft (DFG, German Research Foundation) – Project Number 192346071 – SFB 986 “Tailor-Made Multi-Scale Materials Systems: M^3,” project B4.

Data availability

All relevant data are included in form of Tables and Equations in the present work. Further raw/processed data required to reproduce these findings are available to download from https://www.frontiersin.org/articles/10.3389/fmats.2019.00327/full and the supplementary material provided as link. The raw/processed data required to reproduce the predictions for NPG tomography cannot be shared, see Acknowledgements.

CRediT authorship contribution statement

A. Odermatt: Methodology, Software, Validation, Formal analysis, Visualization, Writing - original draft. **C. Richert:** Methodology, Software, Validation, Formal analysis, Visualization, Writing - review & editing. **N. Huber:** Conceptualization, Funding acquisition, Project administration, Supervision, Writing - review & editing, Methodology, Software, Validation, Formal analysis, Visualization, Writing - original draft, Visualization.

Acknowledgments

Kaixiong Hu and Erica T. Lilleodden are acknowledged for making available the FIB tomography dataset and the FEM solid model of NPG. NH acknowledges discussions with Jörg Weissmüller about the location of the surface for a voxelized structure, which inspired the implementation of the mass-calibration in the FEM voxel models.

References

[1] J. Weissmüller, K. Sieradzki, Dealloyed nanoporous materials with interface-controlled behavior, MRS Bull. 43 (2018) 14–19.
[2] E.T. Lilleodden, P. Voorhees, On the topological, morphological, and microstructural characterization of nanoporous metals, MRS Bull. 43 (2018) 20–26.
[3] H.-J. Jin, J. Weissmüller, D. Farkas, Mechanical response of nanoporous metals: A story of size, surface stress, and severed struts, MRS Bull. 43 (2018) 35–42.
[4] J. Biener, A.M. Hodge, A.V. Hamza, in: Deformation Behavior of Nanoporous Metals. Micro and Nano Mechanical Testing of Materials and Devices, Lawrence Livermore National Laboratory, Livermore, California, 2007, p. 118.
[5] N. Mameka, K. Wang, J. Markmann, E.T. Lilleodden, J. Weissmüller, Nanoporous gold – testing macro-scale samples to probe small-scale mechanical behavior, Mater. Res. Lett. 4 (2016) 27–36.
[6] K. Hu, M. Ziehmer, K. Wang, E.T. Lilleodden, Nanoporous gold: 3D structural analyses of representative volumes and their implications on scaling relations of mechanical behaviour, Phil. Mag. 96 (2016) 3322–3335.
[7] L.-Z. Liu, X.-L. Ye, H.-J. Jin, Interpreting anomalous low-strength and low-stiffness of nanoporous gold: Quantification of network connectivity, Acta Mater. 118 (2016) 77–87.
[8] S. Gnegel, J. Li, N. Mameka, N. Huber, A. Düster, Numerical investigation of polymer coated nanoporous gold, Materials 12 (2019) 2178.
[9] S.S.R. Saane, K.R. Mangipudi, K.U. Loos, J.T.M. De Hosson, P.R. Onck, Multiscale modeling of charge-induced deformation of nanoporous gold structures, J. Mech. Phys. Solid. 66 (2014) 1–15.
[10] K.R. Mangipudi, E. Epler, C.A. Volkert, Topology-dependent scaling laws for the stiffness and strength of nanoporous gold, Acta Mater. 119 (2016) 115–122.
[11] K. Hu, Micromechanical and Three–Dimensional Microstructural Characterization of Nanoporous Gold–Epoxy Composites,, PhD Thesis, Hamburg University of Technology (TUHH), 2017.
[12] C. Richert, N. Huber, Skeletonization, geometrical analysis and finite element modeling of nanoporous gold based on 3D tomography data, Metals 8 (2018) 282.
[13] L.J. Gibson, M.F. Ashby, Cellular Solids Structure & Properties, Pergamon Press, Oxford, 1988.

[14] L. Gibson, M. Ashby, Cellular Solids: Structure and Properties, 2nd. Edn., Cambridge University Press, Cambridge, 1997.
[15] W.E. Warren, A.M. Kraynik, Foam mechanics: the linear elastic response of two-dimensional spatially periodic cellular materials, Mech. Mater. 6 (1987) 27–37.
[16] H. Harders, K. Hupfer, J. Rösler, Influence of cell wall shape and density on the mechanical behaviour of 2D foam structures, Acta Mater. 53 (2005) 1335–1345.
[17] L. Gong, S. Kyriakides, W.-Y. Jang, Compressive response of open-cell foams. Part I: Morphology and elastic properties, Int. J. Solid Struct. 42 (2005) 1355–1379.
[18] L. Gong, S. Kyriakides, Compressive response of open cell foams Part II: Initiation and evolution of crushing, Int. J. Solid Struct. 42 (2005) 1381–1399.
[19] W.-Y. Jang, A.M. Kraynik, S. Kyriakides, On the microstructure of open-cell foams and its effect on elastic properties, Int. J. Solid Struct. 45 (2008) 1845–1875.
[20] W.-Y. Jang, S. Kyriakides, A.M. Kraynik, On the compressive strength of open-cell metal foams with Kelvin and random cell structures, Int. J. Solid Struct. 47 (2010) 2872–2883.
[21] N. Huber, R.N. Viswanath, N. Mameka, M. Markmann, J. Weissmüller, Scaling laws of nanoporous metals under uniaxial compression, Acta Mater. 67 (2014) 252–265.
[22] B. Roschning, N. Huber, Scaling laws of nanoporous gold under uniaxial compression: Effects of structural disorder on the solid fraction, elastic Poisson's ratio, Young's modulus and yield strength, J. Mech. Phys. Solid. 92 (2016) 55–71.
[23] N. Huber, Connections between topology and macroscopic mechanical properties of three-dimensional open-pore materials, Front. Mater. 5 (2018) 69.
[24] C. Richert, A. Odermatt, N. Huber, Computation of thickness and mechanical properties of interconnected structures: accuracy, deviations, and approaches for correction, Front. Mater. 6 (2019) 327.
[25] J. Jiao, N. Huber, Effect of nodal mass on macroscopic mechanical properties of nanoporous metals, Int. J. Mech. Sci. 134 (2017) 234–243.
[26] C. Soyarslan, H. Argeso, S. Bargmann, Skeletonization-based beam finite element models for stochastic bicontinuous materials: application to simulations of nanoporous gold, J. Mater. Res. 33 (2018) 3371–3382.
[27] C. Soyarslan, S. Bargmann, M. Pradas, J. Weissmüller, 3D stochastic bicontinuous microstructures: Generation, topology and elasticity, Acta Mater. 149 (2018) 326–340.
[28] G. Pia, F. Delogu, Nanoporous Au: statistical analysis of morphological features and evaluation of their influence on the elastic deformation behavior by phenomenological modeling, Acta Mater. 85 (2015) 250–260.
[29] T. Hildebrand, P. Rüegsegger, A new method for the model-independent assessment of thickness in three-dimensional images, J. Microsc. 185 (1997) 67–75.
[30] M. Ziehmer, K. Hu, K. Wang, E. Lilleodden, A principle curvatures analysis of the isothermal evolution of nanoporous gold: quantifying the characteristic length-scales, Acta Mater. 120 (2016) 24–31.
[31] Abaqus, Theory Manual, Dassault Systèmes, Providence, RI, USA, 2019.
[32] J. Ollion, J. Cochennec, F. Loll, C. Escudé, T. Boudier, TANGO: a generic tool for high-throughput 3D image analysis for studying nuclear organization, Bioinformatics 29 (2013) 1840–1841.